Temperature-dependent matching in a flux-line lattice interacting with a triangular array of pinning centers without long-range order

J. Eisenmenger,[1,*] M. Oettinger,[1] C. Pfahler,[1] A. Plettl,[1] P. Walther,[2] and P. Ziemann[1]
[1]*Abteilung Festkörperphysik, Universität Ulm, D-89069 Ulm, Germany*
[2]*ZE Elektronenmikroskopie, Universität Ulm, D-89069 Ulm, Germany*
(Received 31 October 2006; revised manuscript received 23 February 2007; published 30 April 2007)

A triangular array of nanoscaled artificial pinning centers (APCs) for magnetic flux lines is prepared into a Nb thin film. The APCs are formed by deposition of Nb onto a Si substrate covered with nanopillars with diameters of 20 nm and lattice constant $a=122$ nm. The production of pillars is based on arrays of gold nanoparticles used as etching masks during reactively ion etching a Si substrate. In this way, the pattern of the original nanoparticle array is transferred onto the substrate. The Au nanoparticles in turn were prepared using the self-organization of inverse micelles formed by diblock copolymers, whose core is loaded with a gold precursor. The resulting lattice of APCs formed by the Si pillars perforating the Nb film mirrors the order of the micellar array which has triangular, short-range order, but loses its directional order for distances larger than about 4–8 lattice constants. Similar to the Little-Parks experiments with external magnetic fields perpendicular to the superconducting film, the resulting $T_c(B)$ curves show ΔT_c deviations. Those vanish for B larger than the first matching field B_1 indicating that no more than one single flux quantum can be captured at each APC, even at low temperatures. Moreover, integer and fractional matching effects in the critical current are observed within a wide temperature range. Two critical currents can be distinguished indicating different types of pinning mechanisms: Strong pinning at APCs and weaker pinning at interstitial sites accompanied by strong caging effects. A unique feature of such prepared samples is the surprising temperature dependence of the matching field for which a value of B_1 is observed close to T_c, which, however, is shifted towards smaller values at lower temperatures. This effect is traced back to a temperature dependent averaging over differently ordered domains within the array of APCs.

DOI: 10.1103/PhysRevB.75.144514 PACS number(s): 74.25.Qt, 74.78.Db, 74.62.−c, 74.78.Na

I. INTRODUCTION

The dynamics of superconducting flux lines still is a fascinating area being both of fundamental and practical interest. Macroscopic behavior and parameters like critical current, flux flow and creep, electrical resistance, and magnetization are strongly influenced by pinning forces between individual flux lines and local inhomogeneities in a superconductor which act as pinning centers. Their strength and spatial distribution not only determine the degree of order of the standard flux-line lattice, but also the resulting vortex dynamics. Enhanced pinning is expected if the flux-line spacing matches the pinning center spacing. Such a matching immediately implies a condition on the applied magnetic field defining the so-called first matching field B_1. For randomly distributed pinning sites the matching condition is met when the flux-line density equals the density of pinning sites.[1] For regular arrays of artificial pinning centers one has a more complex situation,[2] and matching effects are also possible at integer and fractional multiples of B_1. In low T_c superconducting thin films, electron beam lithography and focussed ion beam irradiation has been widely applied to prepare different kinds of pinning centers on a submicrometer scale such as holes[3] (so-called antidots), magnetic dots,[4] nonmagnetic dots,[5] and asymmetric pinning sites.[6,7] Besides matching effects a rich variety of different dynamic phases are expected and observed depending upon applied magnetic field and current.[6–8]

These studies based on conventional lithography methods like electron-beam or focused ion beam lithography, exhibit as a common feature that the artificial pinning centers capture single flux quanta only close to the critical temperature T_c. At lower temperature multiple flux quanta can be pinned by each pinning center because of the corresponding decrease of coherence length that reaches values being considerably smaller than the diameter of the artificial pinning center. To prevent this, centers comparable to the coherence length or smaller are required, which are difficult to produce by conventional lithography techniques.

On the other hand, single-quanta pinning conditions offer the prospect of interesting phenomena related to the interaction of vortices with periodic lattices at low temperatures. For example, a Mott insulator transition between strong and weak Bose glass phases has been studied for systems with randomly arranged columnar pinning[9] and more pronounced effects are expected for pinning lattices with perfect[10] or a certain degree of periodic order.[11] According to simulations by Wengel and Täuber,[11] in a sample with a uniform, random distribution of columnar defects, a Mott insulating phase is not observable as a consequence of the repulsive interactions between vortices. It may, however, persist up to considerably larger interaction ranges, if the disorder distribution is chosen in a more correlated manner, e.g., almost matching the triangular Abrikosov lattice of a pure type-II superconductor. Conversely, a perfect triangular defect lattice would not work at nonzero temperatures either, because of expected correlated hops of flux lines.[11]

Besides these more fundamental aspects, artificial pinning centers in thin films may significantly enhance the critical current densities, thereby providing relevant technological

prospects. To tackle the preparational challenge of obtaining nanoscaled pinning centers, techniques based on self-organization could be of some advantage. In addition to their reduced size, such centers often exhibit a high degree of lateral periodicity with triangular medium-range order resulting from the close packing of the self-assembling units. Thus, this type of ordered array of pinning centers offers strong matching to the triangular vortex lattice that is expected to form under weak native pinning conditions. Although the interaction of such vortex systems with totally random or perfectly periodic pinning centers has been studied extensively, little is known about the interaction of vortices with a lattice of pinning centers exhibiting short-or medium-range order, but no long-range order. This latter situation will be the focus of the present contribution.

To arrive at such arrays of nanoscaled artificial pinning centers (APCs), we presently apply a patterning technique based on self-organization of Au-salt-loaded spherical micelles made of diblock-copolymers that form a triangular lattice of medium-range order over 4–8 lattice constants. By plasma treatments described below, the polymer carriers are completely removed, while the metal salt is reduced to metallic nanoparticles, which still exhibit the original triangular order. Such particles deposited onto Si substrates can be used as an etching mask to provide a corresponding triangular array of Si nanopillars. After depositing a thin Nb film, the pillars perforate the superconducting film thereby defining an array of "antidots" forming the APCs. In this way, large areas of a Nb film (5 mm $\times$ 10 mm) can be patterned with an array of APCs exhibiting a medium-range triangular order with a lattice constant $a \approx 122$ nm. The nanopillars perforating the Nb superconductor have an average diameter of 20 nm delivering, to the best of our knowledge, the smallest antidots ever used as APCs.

From the medium-range order of such APC arrays, one might expect integer and fractional matching. However, since the long-range order is missing, such detailed matching features may be averaged out leaving just one peak of the critical current at B_1. As will be demonstrated below, for quasiperiodic APC arrays as treated here, matching effects become temperature dependent. This is a surprising new feature, since for an ideal APC array the corresponding matching condition is set by its temperature-independent lattice parameter. For a nonperfect APC array, however, different matching conditions must be considered for various subdomains of the lattice exhibiting different orientations and lattice parameters. The overall matching effect then involves additional elastic distortions of the flux-line lattice (FLL) and, thus, will sensitively depend on the ratio of its elastic to its pinning energy, which, in turn, changes with temperature.

II. EXPERIMENT

The APCs are produced by depositing a Nb film onto a Si substrate whose surface was prepatterned with Si nanopillars (height=50 nm, diameter=20 nm, lattice constant $\approx$122 nm) exhibiting a medium-range triangular order. Correspondingly, the resulting superconducting Nb film is perforated with antidots reflecting the order of the nanopillars.

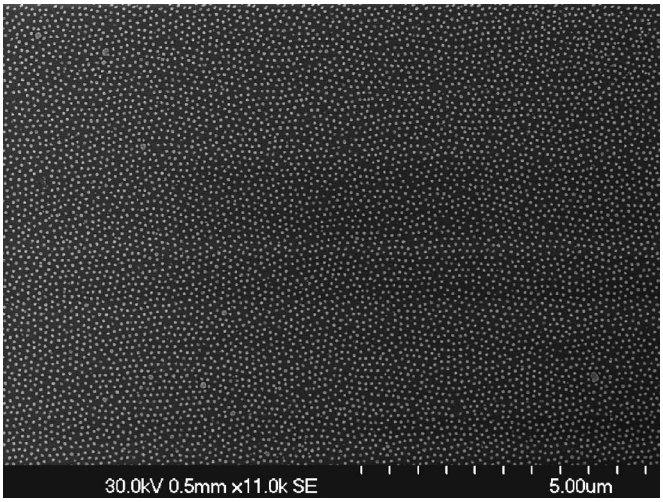

FIG. 1. Scanning electron micrograph of the surface of the Nb layer perforated by an array of Si pillars.

In more detail, the applied patterning process consists of several steps with the first being the deposition of an array of Au nanoparticles onto a Si (100) (5 mm $\times$ 10 mm $\times$ 1 mm) wafer. For this purpose, the substrate is dipped into a toluene solution containing inverse micelles formed by poly(styrene)-*block*-poly(2-vinylpyridine) diblock copolymers. The cores of these micelles are loaded with $HAuCl_4$ as metal precursor. Thus, in standard notation, $PS(1850)$-*b*-$P[2VP(HAuCl_4)_{0.5}(730)]$ in toluene is used. By pulling the substrate out of this solution at an optimized velocity one obtains an approximately close-packed monomicellar layer with a short- or medium-range triangular order. The lattice constant is determined by the block length of the applied polymers, whereas the Au dot size can be varied by the $HAuCl_4$ concentration. By exposing the deposited micelles to a hydrogen plasma (power=30 W, pressure =100 mTorr) for 55 minutes, the polymer matrix is completely removed, the Au salt within the cores is reduced to metallic Au while their arrangement preserves the original triangular order. Exploiting then the Au nanoparticle array as etching mask, in a subsequent step the sample was etched by reactive ion etching in a CHF_3+CF_4 mixture (ratio=10:1, power=30 W, pressure=10 mTorr) for 20 minutes resulting in the formation of Si nanopillars with average heights of 50 nm and diameters of 20 nm. Overgrowing these pillars at ambient temperature with a 50 nm thick Nb layer was achieved by evaporation at a rate of 1 nm/min. Finally, the Nb was covered with a 5 nm thick Au film to prevent oxidation.

Figure 1 shows a scanning electron microscope (SEM) micrograph of the resulting sample surface. The covered pillars are visible as bright spots in the SEM image. Such micrographs can be analyzed further by extracting the distribution of mutual distances of the nanopillars. The result of such an analysis performed on Fig. 1 is presented in Fig. 2, where the solid squares represent the experimental data and the solid curve through them a fit to a Gaussian of the form $n(d)=[(2\pi)^{1/2}\sigma_a]^{-1}\exp[-(d-a_0)^2/(2\sigma_a^2)]$ delivering a maximum at $a_0=121.5\pm0.3$ nm and a width $\sigma_a=16$ nm for the

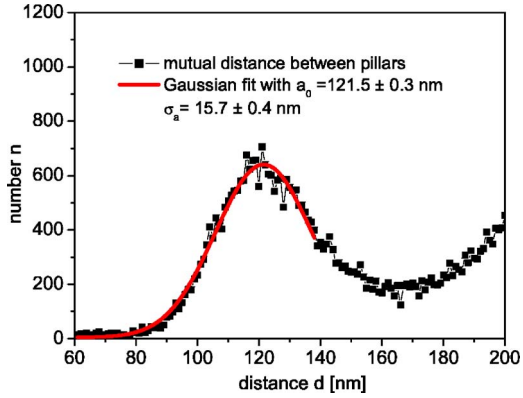

FIG. 2. (Color online) Mutual distance (squares) between APCs calculated from the SEM micrograph Fig. 1. The nearest-neighbor distance has a maximum at 122 nm. From a Gaussian fit (solid line) $n(d)=[(2\pi)^{1/2}\sigma_a]^{-1}\exp[-(d-a)^2/(2\sigma_a^2)]$ the width $\sigma_a=16$ nm is determined.

nearest-neighbor distance. The upturn, starting at 180 nm in Fig. 2, belongs already to the next-nearest-neighbor distance. Assuming a perfectly triangular array, for which $B_1=(2\Phi_0)/(\sqrt{3}a^2)$ with the flux quantum $\Phi_0=2.0678\times10^{-15}$ T m^2, one obtains $B_1=161.74$ mT for $a=a_0$. On the other hand, without assuming any particular order, one calculates a value of 159.29 ± 1.91 mT for B_1 by multiplying the number of pillars in Fig. 1 with Φ_0 and dividing by the area of the SEM image. The error takes uncertainties into account whether pillars at the edge of the SEM image are included or excluded for the calculation. Thus, the values of the first matching field are not significantly different justifying the above approximation of a triangular array.

To demonstrate that the Si nanopillars completely penetrate through the Nb film, a magnified view of an edge of such a film is shown by the SEM image of Fig. 3, from which it is apparent that the pillars are covered by a Nb cap but still perforate the Nb layer. The diameter of the holes in the Nb layer corresponds to the diameter of the Si pillars.

To unequivocally prove the influence of the APCs on the magnetic as well as critical current behavior of the Nb films,

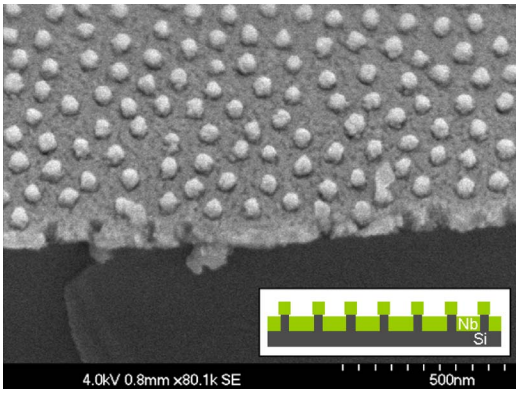

FIG. 3. (Color online) View onto the edge of the tilted sample. The lower dark part is the Si substrate, the upper bright part the Nb layer, which also forms caps on top of the Si pillars. At the edge, holes in the Nb are visible where Si pillars perforate the Nb layer. The inset shows a sketch of the cross section of the sample.

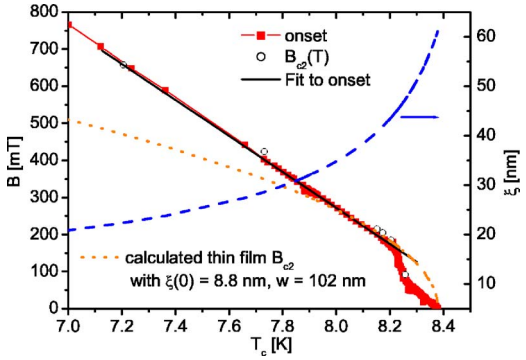

FIG. 4. (Color online) Left-hand axis: $B(T_c)$ determined at the onset of resistive transition for $I=1\times10^{-7}$ A. For comparison $B_{c2}(T)$ is plotted as determined from the field-induced crossover from nonlinear to linear $I(V)$ characteristics. Right-hand axis: The coherence length $\xi(T)$ calculated with $\xi(0)=8.8$ nm. The value of $\xi(0)$ is determined from the linear fit to the onset curve for 7.2 K $<T<$ 8.2 K.

in all cases the results were compared to unpatterned reference samples. For this purpose, only one-half of the Si substrate was nanostructured with pillars, whereas the Nb layer was deposited onto the entire sample guaranteeing identical deposition conditions for patterned and unpatterned parts. For transport measurements the samples were additionally patterned into bridges (width=20 μm, length=50 μm) by optical lithography and reactive ion etching with SF_6. Electrically contacted in a four-probe geometry, $I(V)$ characteristics were determined at different temperatures and magnetic fields applied perpendicular to the sample plane.

Since similar behavior is observed for different samples with slightly different pillar sizes and distances, we will concentrate in the following on the results of a single sample with its reference to allow a better comparison between different experiments.

III. RESULTS AND DISCUSSION

A. Little-Parks effect of critical temperature

The superconducting transition temperature T_c of the sample containing APCs was determined from transport measurements defining the onset temperature by the resistance criterion $R(T_c)=0.9R_0$ with R_0 being the residual normal-state resistance of the sample at low temperatures. In this way, without applying an external magnetic field, a value of $T_c=8.348$ K was obtained for this sample. The corresponding width of the resistive transition (10%–90% of the normal-state resistance) is ≈0.02 K at an applied current $I=1\times10^{-7}$ A. Keeping this current value fixed, the dependence of the critical temperature on the magnetic field was determined with the field oriented perpendicular to the sample plane. The resulting $B(T_c)$ curve is presented in Fig. 4. Alternatively, the boundary $B_{c2}(T)$ between the superconducting and the normal-conducting phase can be extracted from current-voltage $I(V)$ curves taken in various external magnetic fields by defining the crossover from nonlinear to linear behavior of $I(V)$ curves. Indeed, excellent agreement is

observed between the onset $B(T_c)$ and $B_{c2}(T)$.

A linear temperature dependence

$$B_{c2}(T) = \frac{\Phi_0}{2\pi\xi(T)^2} = \frac{\Phi_0(1 - T/T_{c\ \mathrm{Bulk}})}{2\pi\xi(0)^2}, \qquad (1)$$

as expected from Ginzburg-Landau theory for bulk superconductors with critical temperature $T_{c\ \mathrm{Bulk}}$, is observed only for $B > 170$ mT, whereas for smaller fields related to temperatures closer to T_c, the $B_{c2}(T)$ curve significantly deviates from linearity towards smaller values. Such a behavior could be caused by the increasing coherence length close to T_c where it becomes comparable to the width of the superconducting areas between the artificial pinning centers. In that case, the free energy is expected to be changed from its bulk value leading to a nonlinear $B_{c2}(T)$ dependence. In order to investigate this possibility, a straight line is fitted to the experimental $B(T_c)$ curve within the temperature range 7.2 K to 8.2 K (solid line in Fig. 4) delivering the coherence length $\xi(0) = 8.81$ nm and $T_{c\ \mathrm{Bulk}} = 8.56$ K according to Eq. (1). With these parameters the temperature dependence $\xi(T) = \xi(0)/\sqrt{(1 - T/T_{c\ \mathrm{Bulk}})}$ can be calculated and the result is given in Fig. 4 as dashed curve (right-hand scale). Closer inspection of this curve indeed indicates that for $T > 8.2$ K the coherence length $\xi(T)$ becomes comparable to one-half of the distance $w = 102$ nm of the Nb sections between the pillars. Thus, for $T > 8.2$ K the $T_c(B)$ characteristic might be similar to a behavior known from superconducting wire networks[12] and perforated superconducting thin films[13] where periodic Little-Parks oscillations of ΔT_c with integer or fractional number of flux quanta per unit cell are observed, which are superimposed on a nonlinear B^2 dependence of T_c reflecting the finite width of the superconducting wires. It is worth mentioning that the finite width of wires in superconducting networks does not only influence $T_c(B)$ curves but also magnetic moment $m(H)$ curves for which a Gaussian background was found recently.[14]

A parabolic background of the field dependence of T_c is also observed for a single cylinder[15] and is explained by a finite ratio of radius to wall thickness of the cylinder.[16] Additionally, for a perforated thin film the $\sim B^2$ background can be motivated by comparing to the expression of the upper critical field B_{c2} of a thin superconducting film of thickness w in parallel field[13,17]

$$B_{c2}(T) = \sqrt{3}\frac{\Phi_0}{2\pi\xi(T)(w/2)} = \sqrt{3}\frac{\Phi_0\sqrt{(1 - T/T_c)}}{2\pi\xi(0)(w/2)}. \qquad (2)$$

Although the applied magnetic field is normal to the plane of our sample, it is parallel to the Si pillars and therefore parallel to the cylindrical Nb walls around them. Since, the Nb sections between neighboring pillars are smaller than $\xi(T > 8.2\ \mathrm{K})$, the order parameter within these sections may be taken as constant justifying the application of the thin film expression (2). By using $T_c = 8.348$ K, $w = 102$ nm and $\xi(0) = 8.84$ nm, we find the $B_{c2}(T)$ characteristic, which is included in Fig. 4 as the dotted curve and which approaches the measured data points reasonably well between 7.8 K and 8.2 K. The deviation from the measured curve for $T < 7.8$ K mirrors the fact that Eq. (2) is no longer applicable for $\xi(T) < w/2$, and higher correction terms, as well as the bulk expression, must be considered, respectively (cf. Chap. 4.10.2 in Ref. 18). The dotted $B_{c2}(T)$ characteristic is then used as parabolic background reference allowing the definition of additional $\Delta T_c(B)$ deviations by subtracting this background from the measured $T_c(B)$ data. The corresponding results are presented in Fig. 5 as closed squares.

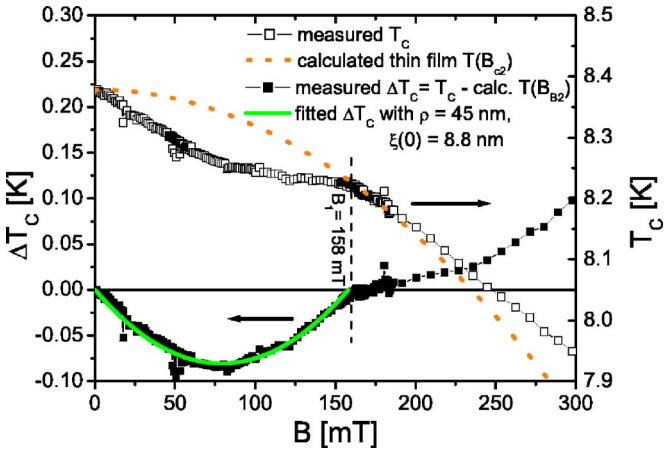

FIG. 5. (Color online) Right-hand axis: Magnification of the low-field regime of Fig. 4, i.e., $T_c(B)$ (open squares) and the calculated, parabolic thin film $T(B_{c2})$ with $\xi(0) = 8.8$ nm, $w = 102$ nm (dotted line). Left-hand axis: Little-Parks deviations $\Delta T_c(B)$, i.e., the difference of T_c and the parabolic background of T_c. Closed squares represent measured data, the solid curve a fit to Eq. (3).

Interpreting these deviations in terms of the Little-Parks effect, for a wire network or a perforated thin film, oscillations are expected as a function of the applied magnetic field. Additionally assuming a phase correlation between the wire loops, the reduction ΔT_c is given by[19]

$$\Delta T_c = -T_c\left(\frac{\xi(0)}{\rho}\right)^2\left[\frac{1}{4} - \left(\frac{\Phi}{\Phi_0} - n - \frac{1}{2}\right)^2\right], \qquad (3)$$

where $\Phi/\Phi_0 = B/B_1$ is the average number of flux lines per hole, n is an integer number with $n < \Phi/\Phi_0 < n+1$, i.e., $n = 0$ for $B < B_1$. In the present case, radius ρ can be approximated by one-half of the lattice constant a, if the superconducting section between the perforated holes is small compared to the hole radius r. In more detail, the radius ρ is expected to be smaller than $a/2 = 61$ nm but larger than the radius of the Si pillars $r = 10$ nm. By fitting Eq. (3) to $\Delta T_c(B)$ for $0 < B < B_1$ we obtain a radius $\rho = 45$ nm which is consistent with this expectation. For the fit we used the fixed values $T_c = 8.348$ K, $\xi(0) = 8.8$ nm, and $B_1 = 158$ mT. The value for B_1 is the position of a sharp peak in $I_c(B)$ characteristics close to T_c, where the matching field could be obtained with a higher precision than from the SEM image (see below). The resulting fit is included in Fig. 5 as solid curve demonstrating excellent agreement with the experimental data up to the first matching field B_1.

For $B > B_1$ a linear $B_{c2}(T)$ characteristic is measured as expected for bulk. That differs from measurements on perforated Nb films deposited onto anodized aluminum

oxide,[13,20,21] where $\Delta T_c(B)$ oscillations with nonlinear B^2 background are measured up to the third matching field. This difference could be caused by the smaller diameters of our APCs at comparable lattice parameter and coherence length. Consequently, the Nb section w between our APCs is larger and $\xi(T)$ becomes smaller than $w/2$ at higher temperatures, i.e., smaller B_{c2} values, than in Refs. 13, 20, and 21. However, $\xi(T) < w/2$ cannot be the only reason for the missing ΔT_c oscillations for $B > B_1$. Even for perforated thin films with well separated holes, Little-Parks oscillations were measured in recent experiments[19] and theoretically predicted.[22–24] In this case the phase correlation between the single loops is absent, and the holes can be considered independently. This results in a $\Delta T_c(B)$ characteristic more similar to the single cylinder in the Little-Parks experiment. Since $\Delta T_c(B)$ changes with the number of flux quanta through the cylindrical hole,[22] we conclude from linear behavior for $B > B_1$, without any $\Delta T_c(B)$ oscillation, that, in our case, the maximum number of vortices which can be captured by a single APC is one.

To a first approximation, we compare this maximum number with theoretical calculations of cylindrical cavities because we are not aware of any expressions which apply to our specific case of Si pillars with Nb caps perforating a Nb film. According to considerations by Buzdin[23] for a triangular array of cylindrical cavities, single quanta pinning is expected if the radius is smaller than a critical value $r_{\text{th}} = (\xi a^2)^{1/3}$. For larger radii multiple vortex pinning becomes more likely. With the coherence length $\xi(0) = 8.81$ nm and a lattice constant $a = 122$ nm of our APC array this radius is $r_{\text{th}} = 50$ nm. An alternative estimation by Mkrtchyan and Shmidt[25] considers a single cavity and not an array which leads to a threshold $r_{\text{th}} = 2\xi = 17.6$ nm. Since the radius of the APCs in our samples is 10 nm and, thus, smaller than both of these r_{th} values, we expect single vortex pinning even at low temperatures, which is consistent with our experimental observation.

B. Matching effect of critical current

Besides $T_c(B)$ curves $V(I)$ characteristics were measured. While the reference sample without APCs shows the expected standard behavior with a continuously changing $V(I)$ curve above a well-defined critical current I_c and a flux flow characteristic before superconductivity breaks down completely, the situation for the sample with pillars is more complex. In Fig. 6 corresponding $V(I)$ curves are presented for $B = 141$ mT and different temperatures. Clearly, two regimes can be distinguished: Coming from small current values, we observe for $I > I_{cn}$ a region which can be described by a linear $V(I)$ characteristic suggesting flux flow. At a second, higher critical current I_{ca}, a kink appears accompanied by a sudden increase of voltage. Similar curves with two different critical currents were observed within a wide range of fields and temperatures. In particular, the two critical currents are observed even for $B < B_1$. In order to properly define these currents I_{cn} and I_{ca}, corresponding voltage criteria must be given. It turns out that for the lower critical current I_{cn} one universal small voltage criterion of 50 nV can be used for all

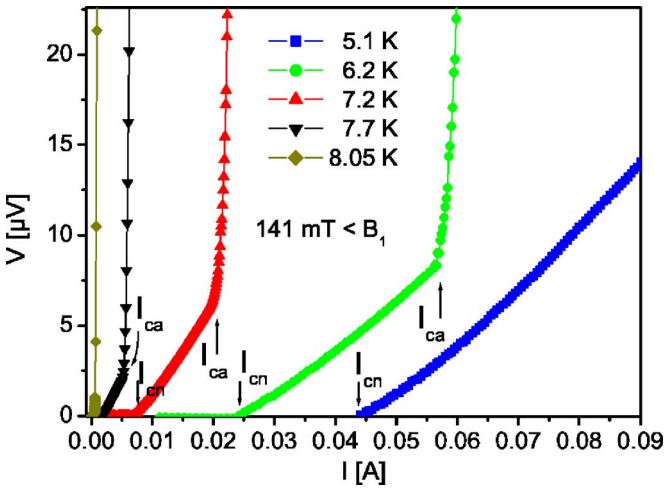

FIG. 6. (Color online) $V(I)$ curves of pillar sample for $B = 141$ mT $< B_1$ and different temperatures. The first critical current is followed by a linear regime before a second critical current appears at I_{ca}.

temperatures. In contrast, for I_{ca} the voltage criterion must be adapted for each temperature to the corresponding kink value. In detail, a voltage criterion was chosen which is slightly larger than the voltage where the I_{ca} kink, i.e., very sudden increase of dV/dI, appears in the $V(I)$ curve. Since these voltages varied with magnetic field, even for constant temperature T, the maximum value was chosen as a voltage criterion for I_{ca} for the specific T. Due to the large dV/dI values for $I > I_{ca}$, this procedure yields I_{ca} values which are practically identical to those determined directly from the step in the different dV/dI curves. However, the used procedure has the advantage to be applicable even at larger magnetic fields, slightly above B_1 and larger, where the kink in $V(I)$ disappears and two different critical currents cannot be distinguished anymore (cf. Sec. III G). Once these criteria are set, the magnetic field dependence of the critical currents can be determined. The results of such measurements taken at $T = 7.21$ K are given in Fig. 7 for both the sample with APCs as well as its reference. The two critical current densities j_{cn} and j_{ca} of the pillar sample are calculated from I_{cn}

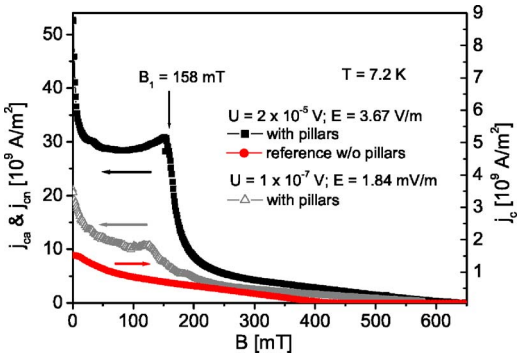

FIG. 7. (Color online) Magnetic field dependence of the critical current densities $j_{ca}(B)$ and $j_{cn}(B)$ as determined from the two voltage criteria given in the inset. Results for the sample with pillars are related to the left scale, those for the reference to the right scale.

and I_{ca} which, in turn, were determined by different voltage criteria. For completeness, the corresponding electrical fields are also given with $E=3.67$ V/m for j_{ca} and $E=1.84$ V/m for j_{cn}. For the reference sample the single critical current density j_c is obtained from the same field criterion $E=3.67$ V/m as for j_{ca}.

Compared to j_c of the reference sample, the pillar sample has a critical current density $j_{ca}(B=0)$ which is more than one order of magnitude larger indicating a strongly increased stability of the vortex system by APCs. These values can be compared with the Ginzburg-Landau depairing current density j_{depair} which can be expressed as a function of the London penetration depth λ and the coherence length ξ (Ref. 17),

$$j_{\mathrm{depair}} = \frac{\Phi_0}{3\sqrt{3}\pi\mu_0\lambda^2\xi}, \tag{4}$$

with flux quantum Φ_0 and the permeability constant μ_0. With $\lambda(0)=150$ nm and $\xi(0)=8.81$ nm, we estimate for the depairing current density $j_{\mathrm{depair}}=1.15\times10^{11}$ A/m^2 at $T=7.2$ K and $B=0$ mT, which is about a factor of 2 larger than j_{ca}.

Besides its higher critical current density, the $j_{ca}(B)$ curve for the sample with APCs in Fig. 7 exhibits a sharp maximum at 158 mT followed by a strong decrease. This value is within the range for the first matching field of 159.29 ± 1.91 mT as estimated from the SEM image Fig. 1. Thus, the maximum is interpreted as a matching effect with j_{ca} being determined by depinning of vortices from *artificial* pinning centers formed by the Si pillars. If the density of Si pillars matches the density of flux lines at the first matching field, an enhanced stability and a pronounced maximum of $j_{ca}(B)$ is expected. Since the peak in $j_{ca}(B)$ is much sharper than the estimation from the SEM image, we will use its position at 158 mT as the value for B_1 in the following.

The lower critical current density j_{cn} can then be attributed to depinning of vortices from additional weaker *native* pinning centers (NPC) and/or by caging. If pinning in the regions between the APCs would only be caused by NPCs, one would expect a monotonous decrease of j_{cn} with B, as opposed to the observation of a small peak close to the matching field B_1. We attribute this effect to caging, i.e., the movement of vortices *between* the APCs is hindered by the repulsive interaction with vortices already pinned at APCs.[26] The efficiency of caging is expected to increase with growing occupation of the APCs by vortices leading to the observed local maximum of j_{cn} close to B_1. At the first glance, interstitial pinning is unexpected for $B<B_1$, because empty APCs are more attractive and at these fields, available. However, simulations for a regular pinning lattice by Reichardt *et al.* show vortices at interstices even below the first matching field.[27] Such a behavior might be even more pronounced if the order is not perfectly periodic and/or pinning by native pinning centers is present.[26]

At this point, it is concluded that both the $\Delta T_C(B)$ deviation for $B<B_1$ and the pronounced matching peak of $I_{ca}(B)$ at B_1 are strong indications that the Nb-capped Si pillars perforating the Nb film act as attractive pinning sites.

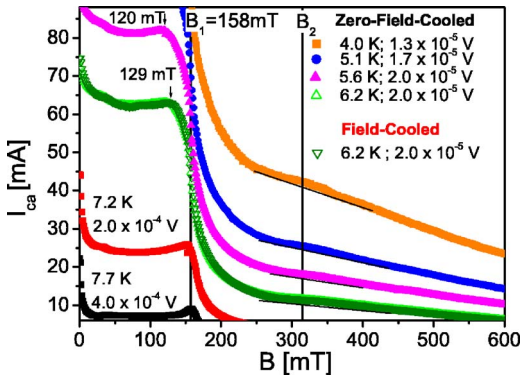

FIG. 8. (Color online) Magnetic field dependence of the second type critical current $I_{ca}(B)$ measured at different temperatures applying the voltage criteria attached to each curve.

C. Temperature dependent matching

A completely new phenomenon is observed when analyzing the temperature dependence of the commensurability effects related to $I_{ca}(B)$. For example, in Fig. 8 $I_{ca}(B)$ curves are presented taken over a temperature range from 4 K to 7.7 K. At the two highest temperatures 7.7 K and 7.2 K, the matching peak of the $I_{ca}(B)$ curve is exactly at B_1, whereas with lower temperature this maximum becomes wider. For significantly lower temperatures $T\leqslant6.2$ K the maximum is shifted to smaller values $B<120$ mT$<B_1$, whereas the steepest decrease remains at B_1. Such a shift of the matching peak is surprising, because the highest stability is expected directly at the matching field B_1 which is given by the temperature independent product of flux quantum Φ_0 with the area density of APCs.

A possible explanation for the shift of matching field could be the influence of flux gradients within the sample which may change with temperature. As numerical simulations show, flux gradients lead to a deviation of the observed matching field compared to that of a homogeneous flux-line density in case of field cooling.[28] Moreover, for decreasing and increasing fields different matching fields could be observed experimentally.[29,30] To estimate a possible influence of flux gradients on the shift of matching field, additional field-cooling (FC) experiments were performed and one example obtained at 6.2 K is included in Fig. 8. Direct comparison, however, of the FC measurements (here the sample is field cooled for each B-field from above T_c to the measuring temperature with no current flowing in the film) to the standard procedure where the sample was zero-field cooled (ZFC) (the external magnetic field is ramped in small steps at constant temperature), proves that the slight differences observed for these two procedures are much too small to account for the above temperature shifts. Similar small deviations between FC and ZFC results were found also at other temperatures pointing to a different mechanism for the observed temperature dependent shift of the matching field.

D. Subareas with different lattice constants

The behavior of vortices pinned by an APC lattice depends on the balance between the energy gained by pinning

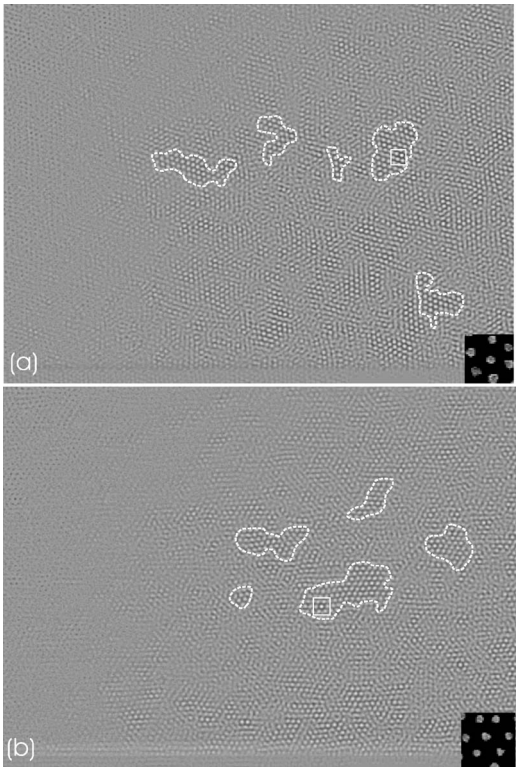

FIG. 9. (a) Autocorrelation image of Fig. 1. The inset shows the chosen subarea and the square its position in the original image Fig. 1. The dashed lines mark examples of ordered domains similar to the pre-selected subarea. (b) Autocorrelation image of Fig. 1. Compared to panel (a) a different subarea is preselected (cf. inset) whose position in the original image Fig. 1 is marked by a square. As a result, the ordered domains are at different locations as compared to (a).

and the elastic energy lost by deforming the vortex lattice from its ideal triangular order. In case of a perfectly ordered triangular APC lattice the vortex lattice is not distorted at the matching field making any additional elastic energy superfluous. The situation changes for a periodic APC lattice containing a certain degree of disorder as in our sample. The kind of disorder becomes apparent in the SEM micrograph of the sample (cf. Fig. 1) where the Si pillars covered with Nb appear as bright dots. On a short-range, the order of pillars is triangular while, on the long-range, periodicity is lost.

This becomes even more obvious in autocorrelation images, where a linear correlation procedure is used to identify areas within a bitmap that are similar to a preselected subarea of the bitmap. Once this subarea is chosen, the algorithm calculates the linear correlation coefficient for each subbitmap of the original image, which has the same dimensions. This yields a two-dimensional map of the correlation coefficient which corresponds to the gray scale values in the autocorrelation image. Bright pixels in this image indicate high correlation and dark pixels show little correlation as the correlation coefficient range of −1 to +1 is mapped from black (equals −1) to white (equals +1) (further details can be found in Ref. 31). Figure 9(a) shows the autocorrelation image of Fig. 1 with a subarea shown in the inset. The lattice constant of this subarea is $a=119.9$ nm and its position in the original image Fig. 1 is marked in Fig. 9(a) by a white square. As examples, the dashed lines mark some of the domains, which appear as ordered in the autocorrelation image, i.e., have identical lattice constants and orientations as the preselected subarea. Areas which appear blurred out have different lattice constants and/or orientation. Similarly, Fig. 9(b) shows the autocorrelation image of the same Fig. 1, but with a different preselected subarea of different lattice constant $a=126.4$ nm. Correspondingly, the positions of the ordered domains are now different from the ones in Fig. 9(a). However, the typical domain diameter of 4–8 lattice constants is comparable in both images.

In the following, we will provide arguments that this kind of disorder, typical for triangular order produced by self-organization, does not result in simply smearing out the matching features, but to the observed shift of matching peak with temperature.

E. Balance of elastic and pinning energy

For simplicity, let us first assume that vortices are pinned only at APCs and there is no pinning on native pinning centers at interstices or by caging. We consider the case where $B=B_1$, i.e., the average density of vortices equals the average density of pinning centers. If we are close enough to T_c or B_{c2}, the vortex lattice can become soft enough that each single vortex is located directly at an individual APC by pinning. For such soft vortex systems a maximum in the $I_{ca}(B)$ curve is observed exactly at $B=B_1$, i.e., local deviations of the APCs from the mean value do not influence the position of the matching peak. The temperature range in which such complete adaptation of the vortex lattice occurs can be estimated from the pinning and elastic energy. We approximate the total pinning energy of N vortices by

$$E_{pin} = N\tfrac{1}{2}\mu_0 H_c^2 \pi r^2 d, \tag{5}$$

where $H_c(T)=\Phi_0/[2\sqrt{2}\pi\mu_0\lambda(T)\xi(T)]$ is the thermodynamic critical field, r the radius of the pinning center, and d the length of the pinning center, which, in the present case, corresponds to the film thickness. The elastic energy can be written as

$$E_{\text{elast}} = \frac{1}{2}\int_{\text{BZ}} \frac{d^3k}{8\pi^3} u_\alpha(\vec{k})\Phi_{\alpha\beta}(\vec{k})u_\beta^*(\vec{k}) \tag{6}$$

with $(\alpha,\beta)=(x,y)$ (Ref. 32). The k integral is over the first Brillouin zone (BZ) of the FLL. The Fourier components $\vec{u}(\vec{k})$ are defined by $\vec{u}(\vec{k})=\frac{\Phi_0}{B}\Sigma_i \int dz \vec{u}_i(z)\exp(-i\vec{k}\vec{R}_i)$, where $\vec{u}_i$ is the displacement of the ith flux line from its ideal position $\vec{R}_i$. The elastic matrix $\Phi_{\alpha\beta}$ is related to the elastic moduli c_{11} for uniaxial compression, c_{66} for shear, and c_{44} for tilt, by

$$\Phi_{xx} = c_{11}k_x^2 + c_{66}k_y^2 + c_{44}k_z^2, \tag{7}$$

$$\Phi_{yy} = c_{66}k_x^2 + c_{11}k_y^2 + c_{44}k_z^2, \tag{8}$$

$$\Phi_{xy} = \Phi_{yx} = (c_{11} - c_{66})k_x k_y. \tag{9}$$

For a first approximation of elastic energy in a thin film, we consider straight and parallel flux lines and only the contri-

bution of isotropic compression in the x and y directions. The distortion is assumed to have single wave number k with amplitude u_0. Then the elastic energy Eq. (6) can be approximated by

$$E_{\text{elast}} = N\frac{1}{2}d\frac{\Phi_0}{B}\mu_0^2[c_{11}(k) - c_{66}]k^2, \tag{10}$$

where $d\frac{\Phi_0}{B}$ is the volume per flux line and $c_{11}-c_{66}$ the modulus for isotropic compression. The moduli c_{11} and c_{66} can be written as[33]

$$c_{11}(k,T) = \frac{B^2}{\mu_0}\frac{1}{(1+k^2/k_\Psi^2)(1+k^2/k_h^2)}\frac{2\kappa^2-1}{2\kappa^2-1+1/\beta} \tag{11}$$

and

$$c_{66}(T) = \frac{B\Phi_0}{16\pi\lambda(T)^2\mu_0}\left(1-\frac{1}{2\kappa(T)^2}\right)[1-b(T)]^2 \times[1-0.58b(T)+0.29b(T)^2]. \tag{12}$$

The functions k_Ψ and k_h are temperature dependent according to

$$k_\Psi(T) = \frac{\sqrt{2[1-b(T)]}}{\xi(T)} \tag{13}$$

and

$$k_h(T) = \sqrt{\frac{[1-b(T)]2\kappa(T)^2}{[2\kappa(T)^2\beta-\beta+1]}}\frac{1}{\lambda(T)}, \tag{14}$$

with $\beta=1.16$ and $b(T)=B/B_{c2}(T)$. Moreover, we used $\lambda(T)=\lambda_{\text{eff}}(0)(1-t^4)^{-1/2}$ and $\xi(T)=\xi(0)(1-t)^{-1/2}$ for the temperature dependence of London penetration depth[32] and coherence length, respectively. With Eq. (5) and (10) the difference between pinning and elastic energy per vortex and length d is

$$\frac{\Delta E(T)}{Nd} \equiv \frac{1}{2}\mu_0 H_c^2\pi r^2 - \frac{1}{2}\frac{\Phi_0}{B}u_0^2[c_{11}(k)-c_{66}]k^2. \tag{15}$$

Figure 10 shows the calculated temperature dependence of the energy difference $\Delta E(T)/Nd$ at $B=B_1$ for parameters of our sample. A typical wave vector k can be approximated by setting $k=2\pi/L$ at which L is 2 times the diameter of an ordered domain as estimated from the autocorrelation images in Fig. 9. Due to uncertainties in the effective penetration depth $\lambda_{\text{eff}}(0)$ and sizes of ordered domains, varying within a finite range, the energy difference was plotted for different values of L, u_0, and $\lambda_{\text{eff}}(0)$. From the distribution of nearest-neighbor distances of pillars, the amplitude of distortion is estimated as $u_0=11-12$ nm (cf. Fig. 2) and 2 times the diameter of ordered domains as $L=(6-12)\,a_0$ (cf. Fig. 9). The other parameters are $T_{c\,\text{Bulk}}=8.56$ K, $\xi(0)=8.81$ nm, $r=10$ nm, and $B=B_1=158$ mT. According to its definition, $\Delta E(T)/Nd>0$ implies that the amount of elastic energy necessary to occupy all the APCs despite their inherent disorder with vortices at B_1 is overcompensated by the gained pinning energy. In those cases, a peak is expected for I_{ca} at a fixed value of B_1. Experimentally, such a behavior is observed for temperatures above 7.2 K, while for lower temperatures the peak is shifted towards lower magnetic fields (cf. Fig. 8). Such a behavior is reflected in the behavior of the $\Delta E(T)/Nd$ curves calculated for various parameters in Fig. 10. Indeed, a crossover of ΔE is observed at a specific temperature depending on the detailed choice of the parameters indicating that the more soft vortices at higher temperatures can adapt to the underlying lattice of APCs, while below the crossover temperature T_x exact matching is no longer energetically favorable. Considering the many approximations used in the calculation, the agreement between the estimated and the experimental T_x values is surprisingly good for parameters u_0 and L, which are within the expected experimental range.

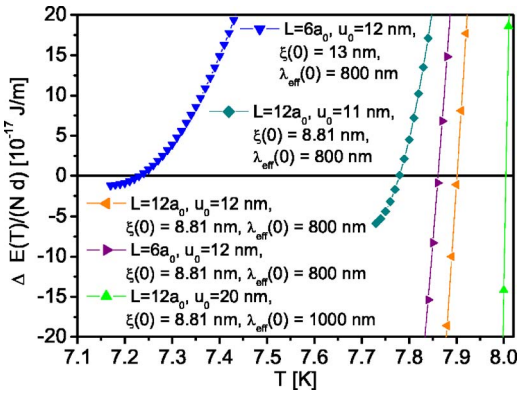

FIG. 10. (Color online) Difference between pinning energy and elastic energy ($E_{\text{pin}}-E_{\text{elast}}$) per vortex and its length d as a function of temperature calculated for different parameters according to Eq. (15). Positive energy differences indicate that the vortex lattice can adapt perfectly to the underlying APC lattice. Negative energy differences indicate that such exact matching is no longer energetically favorable.

Next, the behavior at low temperatures $T \ll T_x$ will be discussed applying ideas from the theory of collective pinning as developed by Larkin and Ovchinnikov.[34] Thus, we adopt the notion of a correlation volume, within which the FLL is reasonably undistorted, but between which there are pinning-induced shear and tilt distortions. Consequently, the macroscopic sample volume is subdivided into correlation volumes with sizes chosen to optimize the trade-off between pinning and elastic energies. The correlation volume increases if the pinning forces are weaker and the elastic moduli are larger. In case of a thin film with the magnetic field normal to the plane, the correlation volume is the film thickness times a correlation area because the elastic modulus for tilt c_{44} can be omitted. In case of Nb films without APCs, Stoddart *et al.*[35] measured correlation radii r_0 within the range from 1.6 μm to 2.4 μm. It is important to note that this range is of the order of the image size given in Fig. 1 showing the APC arrangement within our samples. This comparison especially proves that the expected vortex correlation area is significantly larger than the average size of an ordered APC domain in our sample (cf. Fig. 9). On the other hand, since the density of APCs varies in our sample over a finite range, we have a corresponding distribution of local matching fields $B_{1,\text{local}}$ which can be estimated from the variation of the mutual distances between pillars (Fig. 2). Due to the different length scales of the correlation area and the ordered domains

of APCs, each correlation area of the FLL contains a distribution of local matching fields $B_{1,\mathrm{local}}$. Consequently, even if the magnetic induction B of a correlation area is equal to the geometrically defined average B_1, only part of the flux lines will match the APCs, exactly that part meeting locally the condition $B_{1,\mathrm{local}}=B_1$. Since the FLL is undistorted within the correlation area, regions of the APC lattice, where $B_{1,\mathrm{local}}$ is slightly smaller or larger than B_1, will achieve local commensurability only at slightly smaller or larger B, respectively. Naturally, subareas of the correlation area where B equals $B_{1,\mathrm{local}}$ are optimally pinned. Correspondingly, for subareas with *larger* $B_{1,\mathrm{local}}$ the pinning force is already lower, because not all vortices are at the center of pinning sites. It is important to note that the reduction of pinning forces is not symmetric relative to B_1, since a substantially lower pinning force is expected for subareas in which the flux-line density is *above* $B_{1,\mathrm{local}}$, because the significant increase of weakly pinned vortices at interstitials and their repelling interaction with vortices at APCs result in a less stable state of the entire vortex system.

The critical current I_c in a sample with length l, width w and thickness t is given by

$$\frac{I_c B}{wt} = \frac{F_{\mathrm{total}}}{lwt} = \frac{F_{Vc}}{V_c} \equiv f_{Vc}, \tag{16}$$

where F_{total} is the sum of all pinning forces in the sample and B is the magnetic induction normal to the l-w plane. Thus, $F_{\mathrm{total}}/(lwt)$ represents the pinning force per unit volume, which can be expressed as $f_{Vc}=F_{Vc}/V_c$ where F_{Vc} is the sum of all pinning forces within a correlation volume V_c. As a result, the critical current I_{ca} in our thin film sample depends on the sum of pinning forces within a correlation area. Thus, in order to calculate I_{ca} one needs a model function describing the pinning behavior of an ordered APC domain with a locally defined $B_{1,\mathrm{local}}$. Since at high temperatures close to T_c the vortices can adapt to the APCs, the related, sharply peaked $I_{ca}(B)$ curves like those presented in Fig. 12 below are supposed to represent the pinning behavior within a single highly ordered APC domain. An example for such a $I_{c\,\mathrm{sub}}(B_1,B)$ behavior is shown in Fig. 11 as the dotted curve. Based on this model for each APC domain, the following averaging procedure is applied.

For each ordered FLL domain within a specific correlation volume, the pinning force per unit volume reads $f_{\mathrm{sub}}(B_{1,\mathrm{local}},B)\equiv F_{\mathrm{sub}}(B_{1,\mathrm{local}},B)/V_{\mathrm{sub}}$ with the subvolume V_{sub} given by the corresponding subarea times the film thickness t. To obtain the pinning force per unit volume of the total correlation area $f_{Vc}(B)$, one must integrate over a distribution of $f_{\mathrm{sub}}(B_{1,\mathrm{local}},B)$ curves. To make that procedure work, we assume that the shape of the pinning behavior is practically identical for each ordered domain, as given by the dotted curve in Fig. 11, but with its peak shifted to the local matching field $B_{1,\mathrm{local}}$. Thus, a local pinning force density $f_{\mathrm{sub}}(B_1+\Delta B,B)$ is attributed to the shifted local matching field $B_{1,\mathrm{local}}=B_1+\Delta B$ according to $f_{\mathrm{sub}}(B_1+\Delta B,B)\equiv f_{\mathrm{sub}}[B_1,B(B_1+\Delta B)/B_1]$. We assume further that the distribution of ΔB around $B_1=158$ mT is Gaussian within large enough correlation areas with an estimated range of $\Delta B=\pm 70$ mT and a variance of $\sigma_B=48$ mT. The latter was calculated with $\sigma_B=2(2\Phi_0)/(\sqrt{3}a_0^3)\sigma_a$ where $\sigma_a=16$ nm is the variance of the Gaussian distribution of nearest-neighbor distances as obtained from Fig. 2.

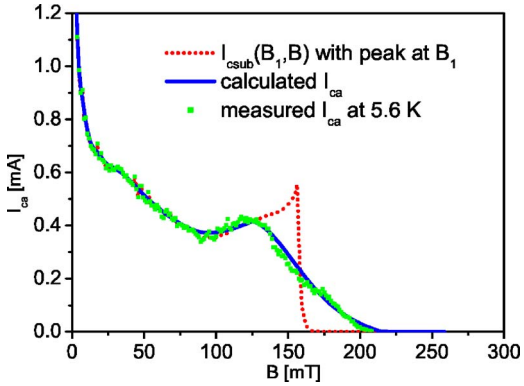

FIG. 11. (Color online) Dotted curve: Model $I_{c\,\mathrm{sub}}(B_1,B)$ curve locally attributed to each ordered APC domain with individual positions of the peak. Solid curve: $I_{ca}(B)$ behavior averaged over a sample according to Eq. (19) with the dotted model function. Filled squares: Measured $I_{ca}(B)$ at 5.6 K.

The pinning force density of a correlation area averaged over all contributing locally ordered domains is then given by

$$f_{Vc} = \frac{\int_{-70\ \mathrm{mT}}^{70\ \mathrm{mT}} d\Delta B \frac{1}{\sqrt{2\pi}\sigma_B} \exp\left(\frac{-\Delta B^2}{2\sigma_B^2}\right) f_{\mathrm{sub}}(B_1+\Delta B,B)}{\int_{\Delta B=-70\ \mathrm{mT}}^{70\ \mathrm{mT}} d\Delta B \frac{1}{\sqrt{2\pi}\sigma_B} \exp\left(\frac{-\Delta B^2}{2\sigma_B^2}\right)}. \tag{17}$$

With (16) and (17) and

$$I_{c\,\mathrm{sub}}(B_1+\Delta B,B) \equiv \frac{f_{\mathrm{sub}}(B_1+\Delta B,B)wt}{B} \tag{18}$$

the $I_{ca}(B)$ curve of the whole sample can be calculated by

$$I_{ca}(B) = \frac{\int_{-70\ \mathrm{mT}}^{70\ \mathrm{mT}} d\Delta B \frac{1}{\sqrt{2\pi}\sigma_B} \exp\left(\frac{-\Delta B^2}{2\sigma_B^2}\right) I_{c\,\mathrm{sub}}(B_1+\Delta B,B)}{\int_{\Delta B=-70\ \mathrm{mT}}^{70\ \mathrm{mT}} d\Delta B \frac{1}{\sqrt{2\pi}\sigma_B} \exp\left(\frac{-\Delta B^2}{2\sigma_B^2}\right)}. \tag{19}$$

This just described procedure was applied to simulate the $I_{ca}(B)$ curve as experimentally determined at 5.6 K, which exhibits a clear shift of its pinning induced maximum towards lower magnetic fields. The corresponding data points are added to Fig. 11 as closed squares with the calculated result given by the solid curve. Excellent agreement is found between both for the parameters given above. Here, it is worth noting that these parameters were not obtained by just fitting but were estimated from corresponding experimentally determined distribution and correlation functions (cf. Fig. 2 and Fig. 9).

There is still another point worth mentioning. Even though a symmetric Gaussian distribution centered at B_1 was used above, this did not result in just broadening the maximum at B_1, but to its shift towards lower B. This shift can immediately be related to the pronounced asymmetry of $I_{c\,\mathrm{sub}}(B_{1,\mathrm{local}},B)$ with its sudden drop for $B>B_{1,\mathrm{local}}$, which is also expected for a transition from a strongly pinned Bose glass to a weakly pinned Bose glass or interstitial liquid.[36] Thus, at this point, the surprising effect of temperature dependent matching fields, which, to the best of our knowledge, has neither been predicted nor observed previously, can be traced back to the following two prerequisites. A nonperfect array of APCs providing locally ordered domains representing local matching fields on a length scale smaller than the correlation area of the vortices and the presence of pinning mechanisms leading to strongly asymmetric $I_{ca}(B)$ curves. The temperature dependence then follows from the changing ratio of pinning to elastic energy of vortices. At high temperatures close to T_c, the FLL can adapt even to the distorted array of APCs due to its elastic softness resulting in a depinning peak at B_1, while at lower temperatures the FLL becomes elastically more and more stiff leading to the necessity to average over locally ordered domains of APCs with their individual matching fields, as described above.

It should be noted that the temperature dependence of the matching peak at B_1 in our experiment differs from the temperature dependence of a peak effect which was theoretically predicted and observed at B slightly below B_{c2} as the FLL softens with the approach to the superconducting-to-normal phase boundary.[34,37] The latter occurs also for completely randomly positioned pinning sites and is not a matching effect at which the number of vortices equals the number of pinning sites at the peak position. Moreover, lowering the temperature increases B_{c2} and the position of the peak shifts to larger B.[34,37] Exactly the opposite occurs in our case where the maximum at the matching field shifts to smaller B at lower temperatures.

F. Interstitial vortices

For simplicity, we neglected in the above discussion that some vortices in an imperfectly ordered lattice are at interstitial sites even below B_1. These vortices are either pinned by native pinning centers or by caging[26] due to the interaction with vortices pinned at APCs. Since the pinning forces of interstitial vortices are smaller than those of vortices pinned by APCs, they are expected to start moving already at lower driving currents. This naturally explains the appearance of two critical currents in Fig. 6, where the lower value at I_{cn} is attributed to depinning from interstitial sites. The movement of these interstitial vortices is characterized by a shifted linear characteristic of type $V=R_{ff}(I-I_{cn})$ which is typical for a flux flow regime where the Lorentz force is large compared to the pinning force resulting in a viscous flow of interstitial vortices. The mean velocity v of vortices gives rise to a drag force $-\eta v$ opposing the sum of Lorentz force and dynamic pinning forces. By expressing the Lorentz force by the applied current I and the pinning force by I_{cn}, the velocity v is given by

$$\eta v = (I - I_{cn})\Phi_0/tw \tag{20}$$

with η is a phenomenological viscosity coefficient, t is the thickness, and w is the width of the microbridge. Along a bridge with length l the moving vortices with area density n_f and velocity v create a voltage V,

$$V = El = vn_f\Phi_0 l. \tag{21}$$

By eliminating v in (21) by (20) the voltage becomes

$$V = R_{ff}(I - I_{cn}) \quad \text{with } R_{ff} = \frac{n_f}{\eta}\frac{\Phi_0^2 l}{tw}. \tag{22}$$

From (22) the area density n_f of moving vortices can be determined if the coefficient η is known. In the Bardeen-Stephen model the flux-flow resistance is determined by the dissipation in the normal-conducting cores by the local time variations of the magnetic field, and is given by

$$R_{ff} = R_0\frac{n_f\Phi_0}{\mu_0 H_{c2}} \tag{23}$$

with R_0 representing the resistance in the normal-conducting state. From (23) the density of moving flux lines n_f can be estimated. For the $V(I)$ curve at $B=141$ mT and $T=6.2$ K in Fig. 6 a density of $n_f=3.4\times10^{-4}B_1/\Phi_0$ is estimated, which is much smaller than the total density of vortices $n_t=B/\Phi_0=0.89B_1/\Phi_0$. Similarly small values for n_f can be estimated for the other temperatures and field values. This small number of moving interstitial vortices is consistent with our observation that the matching peak of I_{ca} fits very well to the density of APCs as determined from the SEM micrograph. If the number of moving interstitial vortices would be significantly larger, the matching peak is expected at larger fields than B_1 because not all APCs would be occupied at B_1.

G. Matching of interstitial vortices

As already mentioned above, the lower critical current $I_{cn}(B)$ is attributed to depinning of interstitial vortices. Surprisingly, this type of vortices exhibits a matching effect as well, even though pinning on native pinning centers should not result in an enhanced stability at B_1. The corresponding experimental results for the relative low temperature of 7.2 K were presented in Fig. 7 and are complemented for higher temperatures in Fig. 12. Here, at 8.05 K and 8.10 K, $I_{cn}(B)$ and $I_{ca}(B)$ curves are shown for immediate comparison. Again, the $I_{cn}(B)$ curves indicate matching effects, which are attributed to caging of interstitial vortices due to the repulsive interaction with those vortices already occupying APCs close to B_1. In agreement with the previous discussion, the $I_{ca}(B)$ curves exhibit peaks exactly at B_1. In contrast, the maximum of the $I_{cn}(B)$ curve at $T=8.05$ K, indicating matching, is shifted down to $B=120$ mT already. At this temperature one approaches the upper limit where the two types of critical currents can clearly be distinguished. Thus, the $I_{cn}(B)$ curve added to Fig. 12 for 8.10 K was determined by formally applying the same voltage criterion as for lower temperatures. In this case, only a kink at a characteristic field below B_1 rather than a peak points to matching.

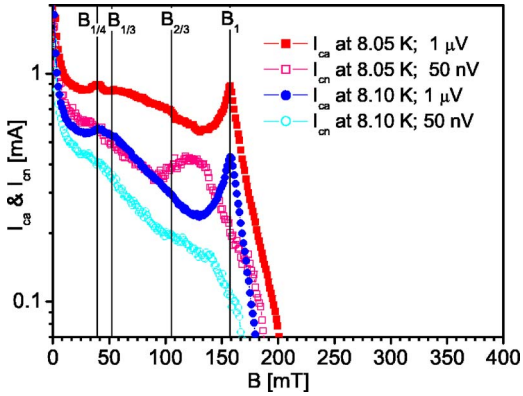

FIG. 12. (Color online) $I_{cn}(B)$ and $I_{ca}(B)$ curves for two different temperatures close to T_c. The applied voltage criteria are given in the inset. Besides integer matching at B_1 also fractional matching at $B_{1/4}$ is observed.

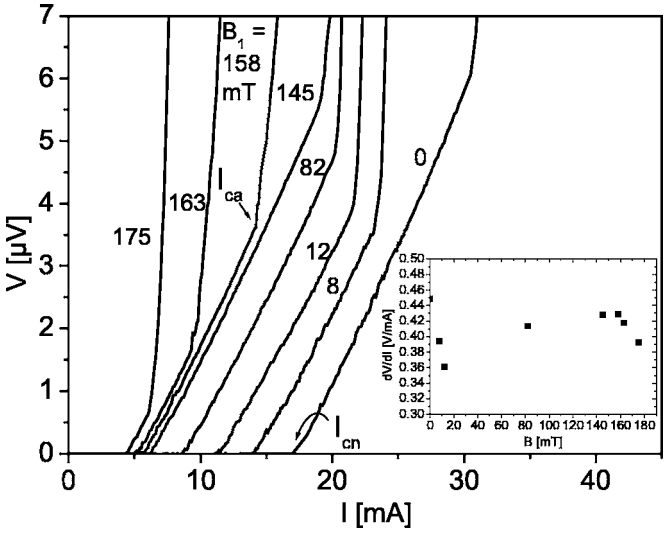

FIG. 13. $V(I)$ curves taken at 7.2 K for various magnetic fields emphasizing the range between I_{cn} and I_{ca} exhibiting a linear behavior with practically constant slope. The numbers denote the magnetic induction in mT. The inset shows $R_{ff}=dV/dI$ for different B.

Remarkably, the largest temperature related shifts observed for the matching maxima of $I_{ca}(B)$ and $I_{cn}(B)$ are comparable with values at about $B=120$ mT. This corresponds to a local lattice constant $a=141$ nm, which fits quite well to the largest measured distances between APCs (Fig. 2). The observation of two different B dependencies of I_{cn} and I_{ca} might be surprising. It may become comprehensible, however, by considering that the ranges of the $V(I)$ curve, at which I_{cn} and I_{ca} are determined, belong to two different dynamical regimes to which differently pinned vortices contribute.

It is worth discussing these two regimes in some more detail. The critical current I_{cn} is determined by the threshold at which the vortices at interstitial sites start to move whereas the vortices at APCs are still strongly fixed. In this regime of interstitial dynamics, the caging pinning potential is determined by the interaction with fixed vortices at APCs. The strongest contribution to this pinning potential comes from occupied nearest-neighbor APCs whose local number increases up to the corresponding local matching fields $B_{1,\mathrm{local}}$, where we expect a maximum of vortex stability. Above $B_{1,\mathrm{local}}$ the number of interstitial vortices increases strongly because all APCs are occupied. This results in a decreasing stability of the interstitial vortex system. Since below and close to B_1, the density of interstitial vortices is still relatively low, the interaction between interstitial vortices is smaller than the interaction with neighboring APC vortices. This is supported by the observation that the measured I_{cn} is considerably smaller than I_{ca} in this regime indicating that the force of caging is smaller than the force which pins vortices directly at APCs. Within this scenario, as soon as the local matching field in the subareas with lowest APC density is reached, the locally increased number of interstitial vortices will give rise to an enhanced vortex flow without being hindered significantly by interstitial vortices in other subareas where the local matching field is not reached, yet. The maximum of $I_{cn}(B)$ at $B=120$ mT, which is approximately temperature independent below 8.10 K, corresponds very well to those subareas with the lowest APC density. For higher densities of interstitial vortices their mutual interaction becomes comparable to that with vortices at APCs. Preferential flow of interstitial vortices is then no longer possible because vortices also will depin from APCs. That occurs for fields slightly larger than the matching field, where the kink in the $V(I)$ characteristic disappears as is demonstrated in Fig. 13. In that situation, vortices at interstitial sites and at APCs depin at one and the same critical current density.

H. B Dependence of R_{FF}

According to the Bardeen-Stephen model, the flux-flow resistance R_{ff} should linearly increase with the areal density of vortices n_f or, equivalently, with the applied B [cf. Eq. (23)]. This expectation, however, is not met by the experiment as is demonstrated in Fig. 13, where $V(I)$ characteristics are presented taken for variable magnetic fields at a fixed temperature of 7.2 K. The current range chosen here emphasizes the regime between I_{cn} and I_{ca} which is attributed to the flow of interstitial vortices as discussed above. While such a flow immediately explains the observed linear characteristics, their constant slope at different magnetic fields is at odds at least with the Bardeen-Stephen model. As already estimated from R_{ff} above, below B_1 the fraction of interstitial vortices is only small. Thus, for $B<B_1$ the constant R_{ff} values may indicate that increasing the magnetic field in this regime leads to a preferential occupancy of APCs rather than interstitials. Here, the primary effect of B is to decrease the volume pinning force resulting in depressed I_{cn} and I_{ca} values and corresponding almost parallel shifts of the characteristics towards smaller currents. For fields B larger than B_1, however, the number of interstitial vortices must increase significantly. Nevertheless, the slopes of the related $V(I)$ curves remain practically unchanged. Comparable behavior was observed within a wide temperature range. One reason could be that the number of actually moving vortices does not increase in the same manner as the number of interstitial vortices. That could occur if only a small number of vortices

contributes to flux flow and most of the additional interstitial vortices, appearing for $B > B_1$, are strongly caged by APCs and do not contribute to flux flow. While such a picture may hold for $B > B_1$, for smaller fields a blocking of flow appears rather unlikely due to the small fraction of interstitials. More likely are contributions of alternative dissipation mechanism for flux flow, like losses induced by irreversible entropy flux in the core vicinity,[38] by nonequilibrium generation and recombination of Cooper pairs around the vortex core,[39] or by nonequilibrium phenomena when vortices cross local pinning potentials.[40,41] From the first two models an increasing R_{ff} with decreasing temperature is expected in contrast to the experimental observations presented in Fig. 6. Thus, an alternative or extended interpretation is required. It could be related to the smaller London penetration depth at lower temperatures causing a better defined caging potential with stronger caging pinning force. If flux-flow viscosity is strongly influenced by nonequilibrium phenomena of vortices crossing local pinning potentials,[40,41] η should increase with this stronger caging pinning force resulting in a smaller R_{ff}. The nearly missing or only slightly increasing R_{ff} with B, in our case, differs from interstitial flow observed by Lange *et al.* for a regular magnetic pinning array on lead.[42] There, the presence of interstitial vortices for $B < B_1$ is observed as vortex creep whereas a linear $V(I)$ characteristic appears only at much larger $B > 2.8B_1$ at which R_{ff} strongly increases with B. A possible origin of these differences is the higher density of our pinning centers from which a different damping behavior becomes likely. In experiments by Villegas *et al.*[6] on a regular array of magnetic, triangular pinning centers in niobium, interstitial flow with ohmic behavior appears at larger fields, i.e., $B > 3B_1$, too. However, any information about a field dependence of R_{ff} is not provided and not further discussed.

I. Integer matching and fractional matching

Besides the commensurability effect at B_1, we also observe multiple integer and fractional matching. However, as opposed to more ideal periodic arrays of APCs, in the present case integer matching is found only up to $B_2 = 2B_1$. An example is given in Fig. 8, where the $I_{ca}(B)$ curves determined for $T \leqslant 5.6$ K show a small but significant shoulder at $2B_1 = 316$ mT whose position is temperature independent. The shoulder is much weaker as compared to the maximum at B_1. This can be caused by the missing long-range order from which matching features at integer multiples of B_1 are expected to be less pronounced. In addition, even in a perfect array, matching features at $B > B_1$ are weaker than at B_1 if each artificial pinning site is able to capture just one single vortex and occupation by multiple flux lines can be excluded.

Besides integer matching, we also observe fractional matching. As demonstrated in Fig. 12 for $I_{ca}(B)$, a local maximum at $B_{1/4} = \frac{1}{4}B_1 = 39$ mT is observed and weaker effects can be supposed at $B_{1/3} = \frac{1}{3}B_1 = 52$ mT and $B_{2/3} = \frac{2}{3}B_1 = 105$ mT. Fractional matching at $B_{1/4}$, $B_{1/3}$, and $B_{2/3}$ is consistent with molecular dynamics simulations by Reichardt and Grønbech-Jensen of triangular arrays of pinning sites.[27] In contrast to the matching peaks at B_1, a clear peak at $B_{1/4}$ is only observed for $I_{ca}(B)$ but not for $I_{cn}(B)$. This indicates that caging has a much weaker influence here than at B_1, which is in fact expected due to larger distances between the vortices involved. Moreover, the number of interstitial vortices does not increase suddenly as at B_1. A further difference compared to B_1 is the temperature independence of the position at $B_{1/4}$, although it becomes broader (Fig. 8). Crucial for the shift of the first matching maximum is a pronounced asymmetry of the local pinning forces of subareas $F_{\mathrm{sub}}(B_{1,\mathrm{local}}, B)$, which strongly decreases at $B_{1,\mathrm{local}}$. This may be attributed to the strongly increasing number of weakly pinned interstitial vortices and their interaction with vortices pinned by APCs. In the vicinity of a fractional matching field such a significant change of the number of interstitial vortices is not expected explaining the temperature independence of this peak.

The present observations differ from experiments on Nb films grown on anodized aluminum oxide (AAO) substrates with larger pores (by about a factor of 2) and comparable antidot distances.[13,20,21,43] In contrast to our electrical transport, Welp *et al.* observe in magnetization measurements matching steps up to the fourth integer order. As discussed in connection with $T_c(B)$, this difference can result from larger APC diameters allowing multiple flux-line trapping per pinning site. Moreover, temperature dependent shifts of matching field were not observed in the AAO samples, which, according to the above discussion, can be attributed to different degrees of order in the APC arrays of AAO and Si pillar samples, respectively.

IV. CONCLUSION

In conclusion, several unexpected features were observed for arrays of APCs produced by a micellar technique, which can be related to their exceptionally small size and the degree of self-organized order of their arrangement.

(i) Due to their nanoscaled size, the APCs guarantee single-vortex pinning even at temperatures well below T_c. This is proven by the fact that the Little-Parks oscillations $\Delta T_c(B)$ can be observed only up to B_1 and not up to higher orders as observed for wire networks or perforated films with larger holes.

(ii) Although the order of the APC array is restricted to short- and medium-range order, integer and fractional matching is clearly observed, even at low temperatures.

(iii) Two types of critical currents, I_{ca} and I_{cn}, could be distinguished, indicating two different types of pinning mechanisms: Strong pinning on artificial pinning centers and weaker pinning by native, randomly positioned pinning centers and by caging in interstitial regions. For magnetic fields slightly larger than B_1, these two critical current densities get indistinguishable because of an increasing number of interstitial vortices and their interaction with flux-lines pinned at APCs.

(iv) The first matching maximum of I_{cn} is at a temperature independent value $B < B_1$ determined by the largest local lattice constant of APCs. In contrast, the position of the first matching maximum of $I_{ca}(B)$ shifts from B_1 at high temperatures to $B < B_1$ at lower temperatures. This effect can be

understood by applying a modified concept of collective pinning. To the best of our knowledge, such temperature dependent effects have not been predicted or observed previously for totally random or perfectly ordered pinning arrays and, thus, must be attributed to the medium-range order of the array of APCs in our sample. They should play a role for other systems as well if the average distance between pinning centers depends on the size of the considered area, which is typical for many self-organized patterns. Such effects should also have relevance for vortex systems interacting with different quasiperiodic pinning arrays[44] for which stability within an extended range of B was predicted, based on physical arguments, and confirmed numerically and analytically.[45]

ACKNOWLEDGMENTS

The authors thank H.-G. Boyen, E. H. Brandt, C. Dietrich, O. Dubbers, B. Koslowski, T. Nattermann, and F. Weigl for helpful and stimulating discussions. The authors gratefully acknowledge the financial support from the Deutsche Forschungsgemeinschaft (SFB 569).

*Electronic address: johannes.eisenmenger@uni-ulm.de

[1] J. Friedel, P. G. de Gennes, and J. Matricon, Appl. Phys. Lett. **2**, 119 (1963); J. Petermann, Z. Metallkd. **61**, 724 (1970).
[2] C. Reichhardt, C. J. Olson, and F. Nori, Phys. Rev. B **57**, 7937 (1998).
[3] M. Baert, V. V. Metlushko, C. D. Potter, E. Rosseel, K. Temst, R. Jonckheere, A. Gilabert, V. V. Moshchalkov, and Y. Bruynseraede, Physica C **235-240**, 2791 (1994); M. Baert, V. V. Metlushko, R. Jonckheere, V. V. Moshchalkov, and Y. Bruynseraede, Phys. Rev. Lett. **74**, 3269 (1995); V. V. Metlushko, L. E. DeLong, M. Baert, E. Rosseel, M. J. Van Bael, K. Temst, V. V. Moshchalkov, and Y. Bruynseraede, Europhys. Lett. **41**, 333 (1998).
[4] Y. Otani, B. Pannetier, J. P. Nozières, and D. Givord, J. Magn. Magn. Mater. **126**, 622 (1993); J. I. Martín, M. Velez, J. Nogués, and I. K. Schuller, Phys. Rev. Lett. **79**, 1929 (1997).
[5] Y. Jaccard, J. I. Martín, M.-C. Cyrille, M. Vélez, J. L. Vicent, and I. K. Schuller, Phys. Rev. B **58**, 8232 (1998).
[6] J. E. Villegas, S. Savel'ev, F. Nori, E. M. Gonzales, J. V. Anguita, R. García, and J. L. Vicent, Science **302**, 1188 (2003).
[7] Y. Togawa, K. Harada, T. Akashi, H. Kasai, T. Matsuda, F. Nori, A. Maeda, and A. Tonomura, Phys. Rev. Lett. **95**, 087002 (2005).
[8] C. Reichhardt, C. J. Olson, and F. Nori, Phys. Rev. Lett. **78**, 2648 (1997); Phys. Rev. B **58**, 6534 (1998).
[9] D. R. Nelson and V. M. Vinokur, Phys. Rev. Lett. **68**, 2398 (1992); Phys. Rev. B **48**, 13060 (1993); M. P. A. Fisher, P. B. Weichman, G. Grinstein, and D. S. Fisher, *ibid.* **40**, 546 (1989); L. Radzihovsky, Phys. Rev. Lett. **74**, 4919 (1995); **74**, 4923 (1995).
[10] L. E. De Long, V. V. Metlushko, S. Kryukov, M. Yun, S. Lokhre, V. V. Moshchalkov, and Y. Bruynseraede, Physica C **369**, 118 (2002).
[11] C. Wengel and U. C. Täuber, Phys. Rev. B **58**, 6565 (1998).
[12] B. Pannetier, J. Chaussy, R. Rammal, and J. C. Villegier, Phys. Rev. Lett. **53**, 1845 (1984).
[13] U. Welp, Z. L. Xiao, J. S. Jiang, V. K. Vlasko-Vlasov, S. D. Bader, G. W. Crabtree, J. Liang, H. Chik, and J. M. Xu, Phys. Rev. B **66**, 212507 (2002).
[14] L. E. De Long, S. Kryukov, V. V. Metlushko, V. V. Moshchalkov, and Y. Bruynseraede, Physica C **404**, 123 (2004).
[15] W. A. Little and R. D. Parks, Phys. Rev. Lett. **9**, 9 (1962).
[16] M. Tinkham, Phys. Rev. **129**, 2413 (1963); R. M. Arutunian and G. F. Zharkov, J. Low Temp. Phys. **52**, 409 (1983).
[17] T. P. Orlando and K. A. Delin, *Foundation of Applied Superconductivity* (Addison-Wesley, Menlo Park, 1990).
[18] M. Tinkham, *Introduction to Superconductivity* (McGraw-Hill, New York, 1996).
[19] A. Bezryadin and B. Pannetier, J. Low Temp. Phys. **98**, 251 (1995).
[20] U. Welp, X. L. Xiao, V. Novosad, and V. K. Vlasko-Vlasov, Phys. Rev. B **71**, 014505 (2005).
[21] W.-K. Kwok, Z. L. Xiao, U. Welp, A. Rydh, V. Vlasko-Vlasov, and V. Novosad, Physica C **412–414**, 347 (2004).
[22] Y. N. Ovchinnikov, Zh. Eksp. Teor. Fiz. **79**, 1496 (1980) [Sov. Phys. JETP **52**, 755 (1980)].
[23] A. I. Buzdin, Phys. Rev. B **47**, 11416 (1993).
[24] A. Bezryadin, A. Buzdin, and B. Pannetier, Phys. Rev. B **51**, 3718 (1995).
[25] G. S. Mkrtchyan and V. V. Shmidt, Zh. Eksp. Teor. Fiz. **61**, 367 (1971) [Sov. Phys. JETP **34**, 195 (1972)].
[26] C. Reichhardt, C. J. Olson, J. Groth, S. Field, and F. Nori, Phys. Rev. B **53**, R8898 (1996); F. Nori, Science **271**, 1373 (1996).
[27] C. Reichhardt and N. Grønbech-Jensen, Phys. Rev. B **63**, 054510 (2001).
[28] C. Reichhardt, J. Groth, C. J. Olson, S. B. Field, and Franco Nori, Phys. Rev. B **54**, 16108 (1996).
[29] A. N. Lykov, Solid State Commun. **86**, 531 (1993).
[30] A. Castellanos, R. Wördenweber, G. Ockenfuss, A. v. d. Hart, and K. Keck, Appl. Phys. Lett. **71**, 962 (1997).
[31] M. Hasselblatt, Autocorrelation Plugin for IMAGEJ, U. S. National Institutes of Health, Bethesda, Maryland, USA, http://rsb.info.nih.gov/ij/plugins/acf.html, 1999; W. S. Rasband, computer program IMAGEJ, U. S. National Institutes of Health, Bethesda, Maryland, USA, http://rsb.info.nih.gov/ij/, 1997–2006.
[32] E. H. Brandt, Rep. Prog. Phys. **58**, 1465 (1995).
[33] E. H. Brandt, J. Low Temp. Phys. **28**, 263 (1977).
[34] A. I. Larkin, Zh. Eksp. Teor. Fiz. **58**, 1466 (1970) [Sov. Phys. JETP **31**, 784 (1970)]; A. I. Larkin and Y. N. Ovchinnikov, J. Low Temp. Phys. **34**, 409 (1979).
[35] S. T. Stoddard, S. J. Bending, R. E. Somekh, and M. Henini, Supercond. Sci. Technol. **8**, 459 (1995).
[36] X. Radzihovsky, Phys. Rev. Lett. **74**, 4923 (1995).
[37] M. J. Higgins and S. Bhattacharya, Physica C **257**, 232 (1996); S. Borka, I. N. Goncharov, D. Fricsovszky, and I. S. Khukhareva, Fiz. Nizk. Temp. **3**, 716 (1977) [Sov. J. Low Temp. Phys. **3**, 347 (1977)].
[38] J. R. Clem, Phys. Rev. Lett. **20**, 735 (1968).

[39] M. Tinkham, Phys. Rev. Lett. **13**, 804 (1964).
[40] S. Pace, G. Filatrella, G. Grimaldi, and A. Nigro, Phys. Lett. A **329**, 379 (2004).
[41] S. Pace, M. G. Adesso, G. Filatrella, G. Grimaldi, and A. Nigro, Physica C **437–438**, 258 (2006).
[42] M. Lange, M. J. Van Bael, A. V. Silhanek, and V. V. Moshchalkov, Phys. Rev. B **72**, 052507 (2005).
[43] U. Welp, Z. L. Xiao, J. S. Jiang, V. K. Vlasko-Vlasov, S. D. Bader, G. W. Crabtree, J. Liang, H. Chik, and J. M. Xu, Physica B **329–333**, 1338 (2003); G. W. Crabtree, U. Welp, Z. L. Xiao, J. S. Jiang, V. K. Vlasko-Vlasov, S. D. Bader, J. Liang, H. Chik, and J. M. Xu, Physica C **387**, 49 (2003).
[44] J. E. Villegas, M. I. Montero, C.-P. Li, and Ivan K. Schuller, Phys. Rev. Lett. **97**, 027002 (2006); M. Kemmler, C. Gürlich, A. Sterck, H. Pöhler, M. Neuhaus, M. Siegel, R. Kleiner, and D. Koelle, *ibid.* **97**, 147003 (2006).
[45] V. Misko, S. Savel'ev, and F. Nori, Phys. Rev. Lett. **95**, 177007 (2005); V. R. Misko, S. Savel'ev, and F. Nori, Phys. Rev. B **74**, 024522 (2006).